



OPEN

Hollow carbon nanospheres/silicon/alumina core-shell film as an anode for lithium-ion batteries

SUBJECT AREAS:

BATTERIES

MATERIALS CHEMISTRY

NANOSCIENCE AND
TECHNOLOGY

SYNTHESIS AND PROCESSING

Bing Li^{1,2}, Fei Yao^{1,2}, Jung Jun Bae^{1,2}, Jian Chang^{1,2}, Mihai Robert Zamfir², Duc Toan Le², Duy Tho Pham^{1,2}, Hongyan Yue^{1,2,3} & Young Hee Lee^{1,2}

¹Center for Integrated Nanostructure Physics, Institute for Basic Science (IBS), Sungkyunkwan University, Suwon 440-746, Korea, ²Department of Energy Science, Department of Physics, Sungkyunkwan University, Suwon 440-746, Korea, ³School of Materials Science and Engineering, Harbin University of Science and Technology, Harbin 150040, People's Republic of China.

Received
19 September 2014Accepted
3 December 2014Published
7 January 2015Correspondence and
requests for materials
should be addressed to
Y.H.L. (leeyoung@
skku.edu)

Hollow carbon nanospheres/silicon/alumina (CNS/Si/Al₂O₃) core-shell films obtained by the deposition of Si and Al₂O₃ on hollow CNS interconnected films are used as the anode materials for lithium-ion batteries. The hollow CNS film acts as a three dimensional conductive substrate and provides void space for silicon volume expansion during electrochemical cycling. The Al₂O₃ thin layer is beneficial to the reduction of solid-electrolyte interphase (SEI) formation. Moreover, as-designed structure holds the robust surface-to-surface contact between Si and CNSs, which facilitates the fast electron transport. As a consequence, the electrode exhibits high specific capacity and remarkable capacity retention simultaneously: 1560 mA h g⁻¹ after 100 cycles at a current density of 1 A g⁻¹ with the capacity retention of 85% and an average decay rate of 0.16% per cycle. The superior battery properties are further confirmed by cyclic voltammetry (CV) and impedance measurement.

Electrochemical energy storage has attracted much attention and received increasing research interest worldwide for a variety of applications such as portable electronic devices and electric vehicles. The lithium-ion battery (LIB) has become one of the most promising energy storage devices because of its relatively high energy density and reasonable rate capability^{1,2}. Since the development of the first commercial LIB in the early 1990s by Sony Energytech³, graphite has been widely used as the anode material. However, the specific capacity of graphite is relatively low due to its intercalation mechanism⁴. To further increase the energy density of LIBs for more demanding applications, novel electrode materials with higher specific capacity are required.

Silicon is an exciting and promising alternative anode material to replace graphite due to its highest theoretical specific capacity of 3579 mA h g⁻¹ among all of the alloy type anodes, which is almost ten times that of graphite anode (372 mA h g⁻¹)⁵. However, two major scientific and technical challenges have hindered its practical applications. First, due to the alloying mechanism, a large number of lithium atoms are inserted into Si and chemical bonds between Si atoms are broken. The structural pulverization induced by the large volume change (>300% at room temperature) during Li insertion and extraction leads to the loss of electrical contact between the active material and the current collector, eventually resulting in capacity fading and short battery lifetime^{6,7}. Second, due to the volume expansion and shrink, a thick solid-electrolyte interphase (SEI) layer can be formed deriving from the irreversible side reactions with the organic electrolyte⁸. This causes the degradation of battery performance due to the consumption of electrolyte and lithium ions, the electrically insulating nature and the rather long lithium diffusion length through the thick SEI⁹. Thus, to make silicon a good anode candidate for LIBs, two major issues must be settled: minimizing the degradation of the mechanical integrity and maintaining the stability of the SEI.

Numerous works have been conducted on the research of silicon anode to meet the above challenges. Reducing the size of active materials into nanoscale could be one efficient way to alleviate the mechanical fracture. Various structures synthesized by different methods have been proposed, including nanoparticles^{10,11}, nanotubes^{12,13}, nanowires^{14,15}, nanospheres¹⁶, core-shell nanofibers^{17,18} and thin films¹⁹. These nanostructures have demonstrated superior performance compared to bulk silicon because of their ability to release the strain. Moreover, nanostructured silicon has settled the issue of the active material detachment from the current collector, resulting in significant improvement of electrochemical cycling. In spite of this, the surface of silicon is still directly exposed to the electrolyte and therefore unstable SEI is still formed.



To tackle this problem, conformal coatings on silicon anode have been explored. Amorphous carbon is a good candidate and often used as a coating layer because of the relatively simple and inexpensive fabrication process, and more importantly it is both electronically and ionically conducting²⁰. Recently Al_2O_3 was used as a coating material fabricated by atomic layer deposition (ALD)^{21–23}. ALD is a mature technique for conformal coatings. The process is quite easy and the thickness of the deposited materials can be well controlled. Metallic and SiO_x coatings have also been studied^{9,24}. These coatings prevent silicon from being exposed directly to the electrolyte. As a result, a thin SEI layer can be formed. Nevertheless, in some cases, these coatings will fracture upon the volume expansion of silicon, and therefore the silicon surface will be exposed to the electrolyte again. To maintain a stable SEI layer on the surface of the electrodes, void space around silicon inside the coatings is necessary to be built. Recently, numerous relevant structures have been designed to fulfil this requirement^{25–35}. The free volume allows silicon to expand without rupturing the outer coating layers, and thus the stable SEI is possibly maintained.

In this report, hollow carbon nanospheres/silicon/alumina (CNS/Si/ Al_2O_3) core-shell structure was fabricated to overcome the above issues. The CNS thin film substrate was fabricated by electrophoretic deposition technique, followed by the deposition of amorphous Si and Al_2O_3 thin layer. The CNS/Si/ Al_2O_3 hollow structure not only provided a conductive film connecting a series of CNSs into 3D network, but also accommodated large silicon volume expansion due to the existence of void space provided by CNSs. Moreover, the electrochemical performance was further improved by the reduced SEI formation due to the coated Al_2O_3 layer and the efficient electron transport facilitated by the surface-to-surface contact mode.

Results

The fabrication process of CNS/Si/ Al_2O_3 is described in Fig. 1. Hollow CNSs were synthesized by the template-directed carbon segregation method using nickel nanoparticles (Ni-NPs) as a template^{36,37}. The CNS 3D substrate was fabricated on stainless steel current collector by electrophoretic deposition technique³⁸. Amorphous Si was then deposited on the surface of CNSs through plasma enhanced chemical vapour deposition (PECVD). A thin layer of Al_2O_3 (~ 6 nm) was finally deposited by ALD. The thickness of Al_2O_3 layer was critical and should be optimized because of trade-off phenomenon between maintaining the mechanical and chemical stability and decreasing ionic resistance. Several advantages are expected from as-fabricated nanostructure. First, as a novel 3D substrate, the CNSs are interconnected, ensuring high conductivity for electron transport. Second, the CNS/Si/ Al_2O_3 structure can efficiently accommodate the large volume change of Si due to the existence of void space provided by hollow CNSs. The inward expansion is possible because the outer shell of Al_2O_3 layer is mechanically rigid while both carbon and silicon layers are considerably softened with significant amount of Li insertion⁹. Third, during lithiation and delithiation, Al_2O_3 coating is not fractured due to the inward expansion, and thus silicon is not in contact with the electrolyte. The interface with the electrolyte is mechanically constrained and remained static, and as a result, the reduction of SEI formation is expected. Fourth, void-involved Si/C nanohybrids are well studied, where Si is in general encapsulated within hollow carbon matrices, and point-to-point or line-to-line contact is formed at the interface between silicon and carbon^{25–29}. These contact modes would retard the fast transport of electrons due to the limited contact area. In our design, silicon is coated on the outer surface of hollow CNSs, which

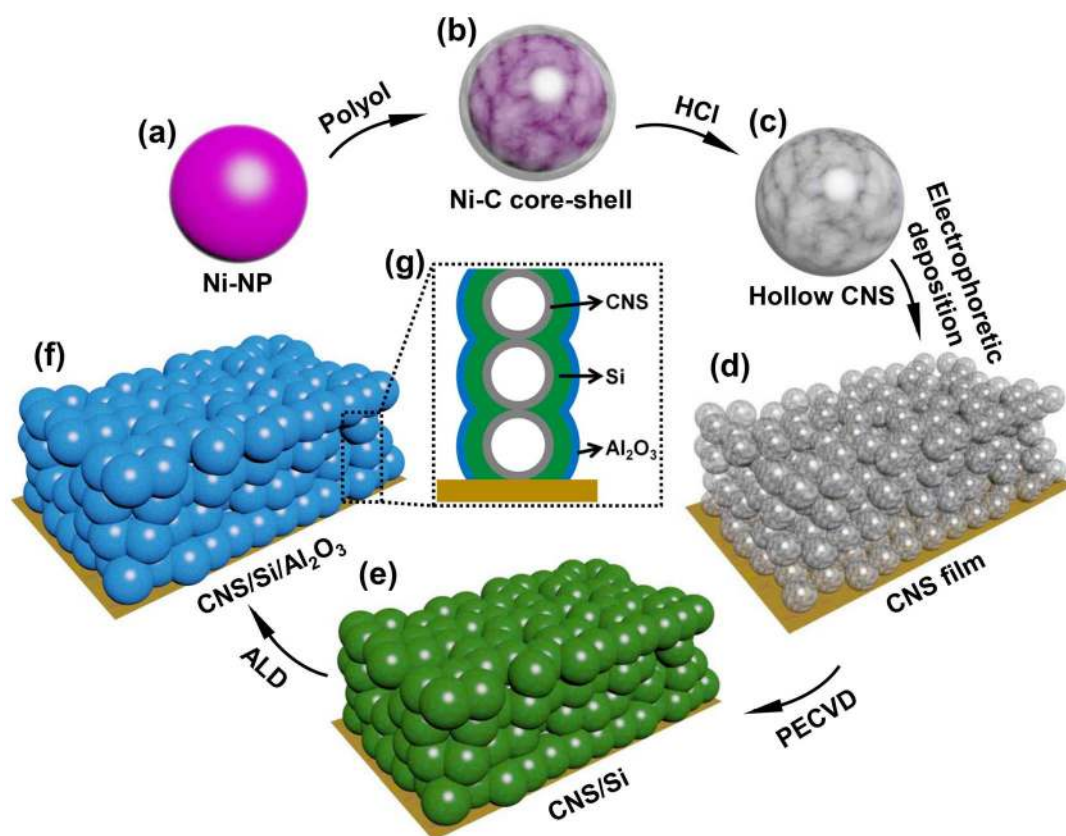


Figure 1 | Schematic of hollow CNS/Si/ Al_2O_3 core-shell film fabrication processes. (a) Ni-NPs prepared by solution reaction. (b) Ni-C core-shell structure fabricated by template-directed carbon segregation method. (c) Hollow CNSs obtained after HCl etching. (d) CNS film deposited on stainless steel by the electrophoretic deposition technique. (e) CNS/Si obtained after silicon deposition with PECVD. (f) CNS/Si/ Al_2O_3 obtained after Al_2O_3 deposition with ALD. (g) The inner structure of CNS/Si/ Al_2O_3 .

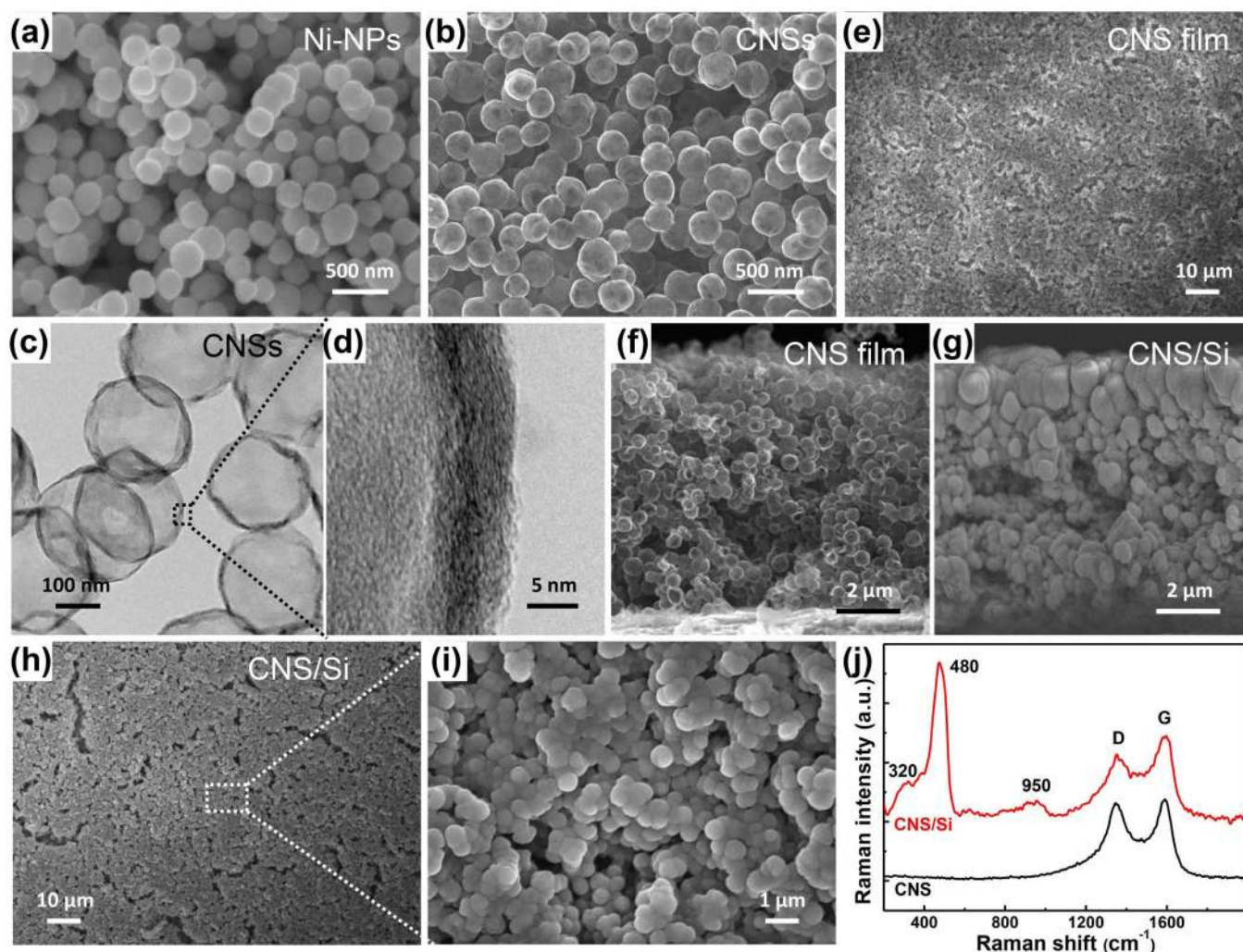


Figure 2 | Characterization of Ni-NPs, CNSs and CNS/Si. (a) SEM image of Ni-NPs with average diameter of 300 nm. (b) SEM (c) TEM and (d) HRTEM images of hollow CNSs with wall thickness of 8 nm. (e) Top view and (f) side view SEM images of CNS film on stainless steel. (g) Side view and (h, i) top view SEM images of CNS/Si. The thickness of the CNS/Si film is about 8–9 μm . (j) Micro-Raman spectra of CNS and CNS/Si films.

enables the surface-to-surface contact and thus the contact area is maximized. As a consequence, our structure exhibits high specific capacity, superior cycle ability and rate capability.

Figure 2a shows the scanning electron microscopy (SEM) image of Ni-NPs with an average diameter of 300 nm. Hollow CNSs were obtained after HCl etching of the carbon-encapsulated Ni-NPs and maintained the original shape and size of the Ni-NPs without being collapsed, as seen in Fig. 2b. To demonstrate the hollow structure, the transmission electron microscopy (TEM) image of CNSs was displayed in Fig. 2c, where void space can be observed. Figure 2d is the high-resolution TEM image of CNSs, which showed that the wall thickness was about 8 nm. The CNS film was fabricated on the current collector using electrophoretic deposition technique. From the top view SEM image (Fig. 2e) we observed that small cracks existed all over the film, which were formed during the drying process after electrophoretic deposition due to the tension change. The thickness of the film was about 8–9 μm , as shown in the side view SEM image (Fig. 2f). Moreover, the CNSs still maintained their spherical shape after electrophoretic deposition. CNS/Si film was obtained after amorphous Si growth with PECVD. Figure 2g presents the side view SEM image of CNS/Si. As seen in the image, more Si was deposited on the top layer of the film. This was ascribed to the limited accessibility of Si atoms during PECVD. From the top view SEM images of CNS/Si (Fig. 2h and 2i), we observed that Si was deposited

uniformly on the surface of CNSs, and in addition, cracks also appeared on the film following the original texture of the CNS film. These cracks were beneficial to the electrochemical cycling because they can further accommodate the volume change of the electrode.

Micro-Raman spectra of CNS and CNS/Si film in Fig. 2j clearly exhibits G band near 1595 cm^{-1} indicating sp^2 hybridization of carbon network and D band near 1352 cm^{-1} showing the defects in the structure³⁹. The intensity ratio of D band to G band (I_D/I_G) of CNS/Si film (~ 0.78) was smaller than that of CNS film (~ 0.95), suggesting an improved graphitization in the CNS network after Si deposition. Meanwhile, three Si-related peaks were shown in the spectrum of CNS/Si. The broad peak located at around 480 cm^{-1} was assigned to amorphous Si (a-Si). The peak near 320 cm^{-1} resembled the second-order transverse acoustic phonon mode of crystalline Si (c-Si) and could be softened in a-Si^{40–42}. In addition, the small peak at 950 cm^{-1} was contributed from the chemisorbed atomic/molecular oxygen species⁴³.

Figure 3a shows the SEM image of CNS/Si/ Al_2O_3 . No obvious change can be observed on the morphology before and after ALD process since Al_2O_3 layer was very thin. To demonstrate the structure, we conducted TEM analysis. A 6 nm thick layer of Al_2O_3 on the surface can be distinguished by contrast from the TEM image in Fig. 3b, and the inset of the selected area electron diffraction (SAED) pattern verified the amorphous nature of Si. Figure 3c exhi-

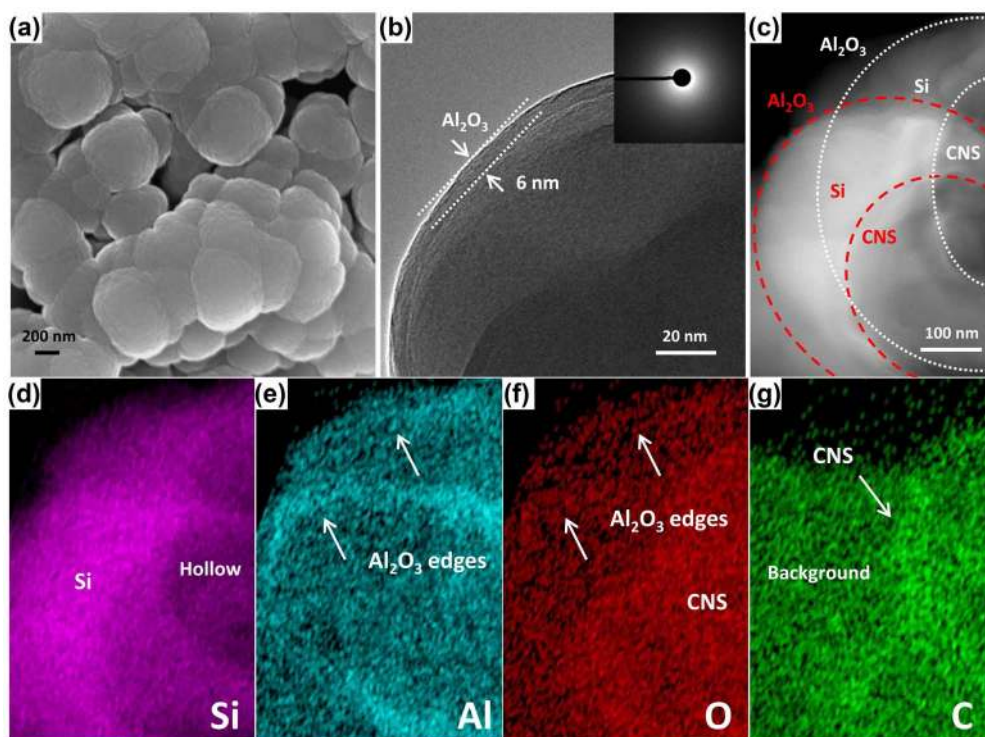
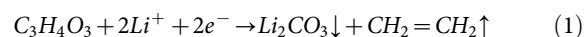


Figure 3 | SEM and TEM characterization of CNS/Si/Al₂O₃. (a) SEM and (b, c) TEM images of CNS/Si/Al₂O₃. A ~ 6 nm thick layer of Al₂O₃ can be distinguished by contrast on the surface of the sample in (b), where the SAED pattern of silicon was shown as well in the inset. EDX element mapping of CNS/Si/Al₂O₃ from (c) revealing the elemental distribution of (d) Si, (e) Al, (f) O, and (g) C.

bits the TEM image of two overlapped CNS/Si/Al₂O₃ particles, where the hollow core-shell structure can be clearly observed. The energy dispersive X-ray (EDX) element mappings are listed in Fig. 3d–g, revealing the elemental distribution of Si, Al, O and C, respectively. Hollow structure was seen from the Si mapping, and the Al₂O₃ coating can be distinguished from the Al and O mapping. Due to the functionalization process, the CNSs contained certain amount of oxygen, as shown in the O mapping. Because TEM was taken using the holey carbon coated copper grid, the C mapping simply revealed the background interference. Nevertheless, CNSs can still be identified from the image.

To understand the lithiation and delithiation processes of different electrode materials in detail, we investigated the cyclic voltammetry (CV) measurement systematically. Each test was conducted in a coin-type LIB for 10 cycles with a potential window of 0.01~1 V at 1 mV s⁻¹. Figure 4a–c show the CV curves of the 2nd, 5th and 10th cycles of Si film, CNS/Si and CNS/Si/Al₂O₃, respectively. Si film was deposited directly on stainless steel without the CNS substrate using the same PECVD conditions. Cathodic peaks at 0.01 V, 0.08~0.09 V, 0.19~0.21 V and 0.34~0.36 V, and anodic peaks at 0.34~0.38 V and 0.50~0.52 V were observed. The cathodic peak at 0.08~0.09 V came from CNSs in the composite. The cathodic peaks at 0.19~0.21 V (corresponding to the transition from a-Si to a-Li_xSi) and 0.01 V (a-Li_xSi to c-Li₁₅Si₄), and the anodic peaks at 0.34~0.38 V (c-Li₁₅Si₄ to a-Li_xSi) and 0.50~0.52 V (a-Li_xSi to a-Si) were characteristic peaks for amorphous Si. The cathodic peak at 0.34~0.36 V was due to the SEI formation^{44,45}. Al₂O₃ was electrochemically inactive and did not contribute to the CV curves under our experimental conditions. In Fig. 4a, the intensity of all the peaks decreased as the cycle number increased, indicating the instability of the Si film electrode. In the 2nd cycle in Fig. 4b, the lithiation peak for CNSs did not appear. This was attributed to the fact that during the first two cycles, Li⁺ had not penetrated into the CNSs yet. Later in the 5th and 10th cycles, one new cathodic peak at 0.09 V was observed, ensuring the electrochemical contribution of CNSs. The intensity of

the characteristic peaks did not change much throughout 10 cycles, demonstrating that the hollow CNS substrate was highly conductive and accommodated the volume expansion of Si, and thus quite stable electrochemical performance was delivered. However, an obvious peak at 0.34~0.36 V related to the unstable SEI formation appeared from the 2nd to 5th cycle. SEI consists of several kinds of solid state components. Li₂CO₃ has been considered from the decomposition of the solvent (take ethylene carbonate as an example)²²:



In addition, LiF is believed to be formed from the reduction and decomposition of LiPF₆:



Figure 4c displays the CV curves of CNS/Si/Al₂O₃ electrode. In the 2nd cycle, the characteristic peaks of Si were not so obvious, and in the later cycles the intensity of almost all the peaks kept increasing, indicating full activation of Si. It has been reported that Al₂O₃ reacted with Li⁺ and LiAlO₂ or Li_xAl₂O₃ was formed at the top surface during cycling, which substantially conducted Li⁺⁴⁶. In the first few cycles, Al₂O₃ layer consumed certain amount of Li⁺ that did not contribute to the curves. Li⁺ penetrated the Si layer and inserted into CNSs in the 10th cycle where the CNSs-related peak at 0.08 V finally appeared. The same trend has also been observed elsewhere^{22,26}. The increase of peak intensity here also suggested that the Al₂O₃ layer became more and more ionically conductive. SEI formation peak disappeared, in good contrast to that of CNS/Si shown in Fig. 4b. Since the insulating Al₂O₃ layer suppressed electron transfer from Si to electrolyte, electron-free equation (3) was the only possible mechanism to occur. Thus only a small amount of LiF was

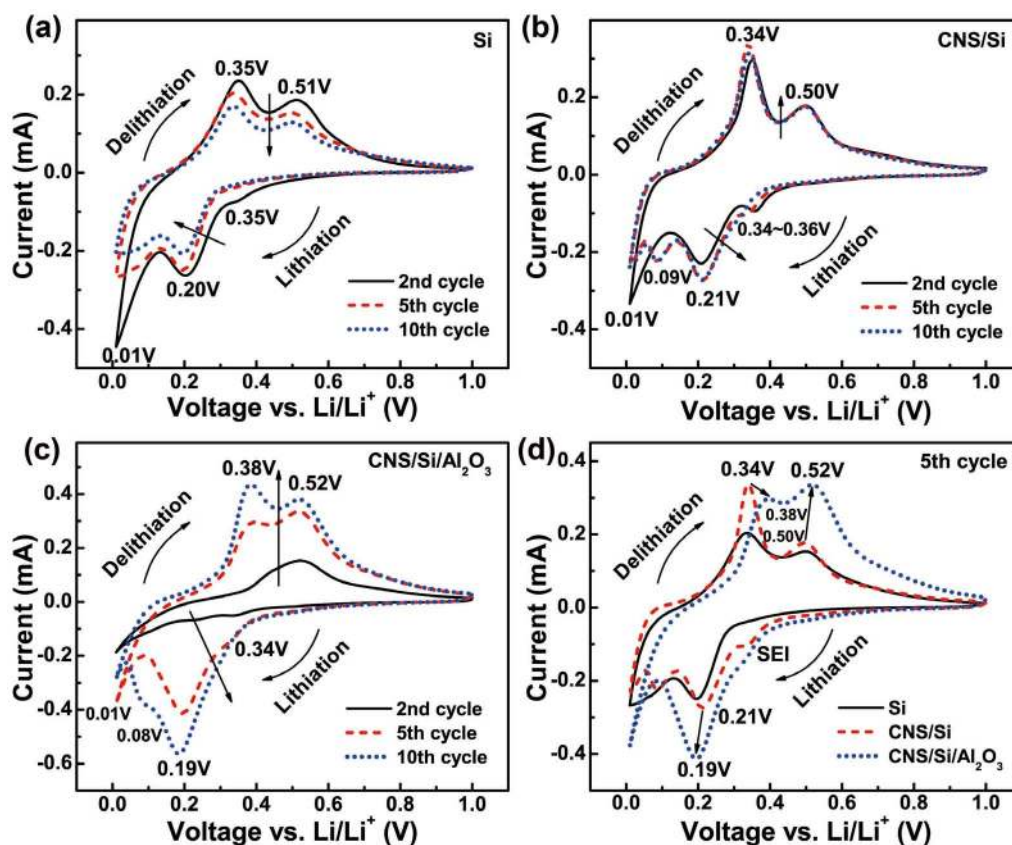


Figure 4 | CV characterization of different electrodes. CV curves of the selected cycles of (a) Si film, (b) CNS/Si and (c) CNS/Si/Al₂O₃ between 0.01~1 V at 1 mV s⁻¹. (d) CV curves of the 5th cycles of each electrode. The characteristic peaks for CNS, Si and SEI formation are indicated. The peak shift between CNS/Si and CNS/Si/Al₂O₃ is also shown in (d).

formed due to the decomposition of LiPF₆ with heat and moisture. Since this process did not involve Li⁺, this may not appear in CV curves, as shown in Fig. 4c. No Li₂CO₃ was formed, unlike conventional SEI formation on Si surface. Therefore, the decomposition of electrolyte was significantly reduced in the case of Al₂O₃ overlayer deposition. In Fig. 4d, the CV profiles of the 5th cycles for the three electrodes discussed above were drawn together to compare the difference of peak position. The alloying and dealloying voltages for Si and CNS/Si were almost the same, while those of CNS/Si/Al₂O₃ were slightly different. The Al₂O₃ coating has changed the electrochemical properties of the anode material to some degree. For example, the peak potential of alloying for CNS/Si was 0.21 V, and it was pushed down to 0.19 V after 6 nm Al₂O₃ layer was coated on Si. Delithiation peaks presented the similar trends: 0.34 to 0.38 V and 0.50 to 0.52 V. Similar phenomenon has been observed elsewhere^{22,46}.

Next, the electrochemical properties of different anodes were evaluated using galvanostatic charge/discharge cycles with a potential window of 0.01 to 1 V. The specific capacity values reported here were calculated on the basis of the entire electrode weight, unless specified. The charge/discharge profiles for different cycles of CNS/Si and CNS/Si/Al₂O₃ are shown in Fig. 5a and 5b, respectively. Current densities of 0.2 A g⁻¹ for the 1st cycle, 0.5 A g⁻¹ for the 2nd and 3rd cycles and 1 A g⁻¹ for the rest cycles were applied for the battery test. All of the profiles were very similar, in good agreement with the behaviour of amorphous Si and carbon. For instance, the lithiation potential displayed the plateau profiles at ~0.2 V (Si) and ~0.1 V (CNSs), while the delithiation process exhibited two plateaus at ~0.3 V and ~0.5 V (Si). The initial discharge capacities of the two anodes were similar: 2170 mA h g⁻¹ for CNS/Si and 2055 mA h g⁻¹ for CNS/Si/Al₂O₃. Considering the Si mass percent of 62.9% and 62.5%, the initial discharge capacities based on the Si mass were

actually higher: 3435 mA h g⁻¹ and 3273 mA h g⁻¹, respectively. However, the specific capacity of CNS/Si fell behind after 100 cycles.

Figure 5c displays long term charge/discharge capacity of four electrodes: Si film (black squares), CNS/Si with Si mass percent of 22.1% (red circles), 62.9% (blue triangles) and CNS/Si/Al₂O₃ with Si mass percent of 62.5% (green stars). The initial charge and discharge capacities of Si film were 4180 mA h g⁻¹ and 3200 mA h g⁻¹ at a current density of 0.2 A g⁻¹, which were close to the theoretical value. However, the capacity was reduced to ~500 mA h g⁻¹ only after 20 cycles, indicating the fracture of the structure. The discharge capacity crashed down to 40 mA h g⁻¹ after 100 cycles with only 3.2% of the initial capacity retained. CNS/Si (22.1%) did not exhibit high reversible capacity due to the low Si content. However, it presented much higher capacity retention (82.0%) after cycling, verifying that the hollow CNS substrate did play a valuable role in the electrochemical process. When the Si mass percent was increased to 62.9%, the specific capacity also went up. Nevertheless, the capacity decayed faster and only 64.8% discharge capacity retention was obtained after 100 cycles. Thicker Si film suffered more structural pulverization due to larger volume expansion. As a consequence, thicker SEI layer was formed, leading to the degradation of battery performance. Eventually 6 nm Al₂O₃ layer was deposited on the surface of Si, and the sample with similar Si weight content (62.5%) exhibited excellent battery performance. As displayed in the figure, the initial capacities were almost the same between CNS/Si (62.9%) and CNS/Si/Al₂O₃ (62.5%), which were 1760 mA h g⁻¹ and 1840 mA h g⁻¹ at the 4th cycle, respectively. After about 20 cycles the capacity of CNS/Si/Al₂O₃ kept steady while that of CNS/Si continuously declined. The discharge capacity reached 1560 mA h g⁻¹ after cycling with a retention of 84.8% and a capacity decay of 0.16% per cycle for CNS/Si/Al₂O₃. From the capacity based on Si mass of the above three

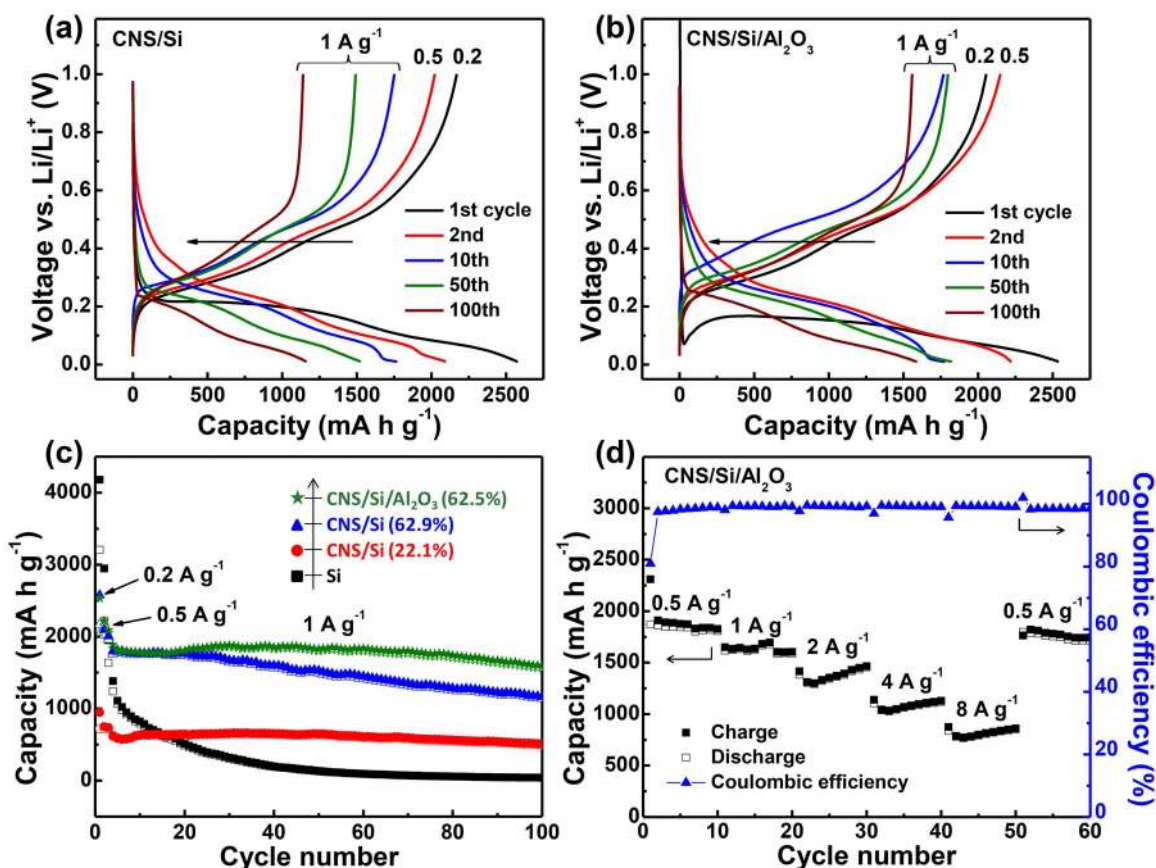


Figure 5 | Electrochemical characterization of different electrodes. Voltage profiles of (a) CNS/Si and (b) CNS/Si/Al₂O₃ with the potential window of 0.01~1 V. The current densities are 0.2 A g⁻¹ for the 1st cycle, 0.5 A g⁻¹ for the 2nd and 3rd cycles and 1 A g⁻¹ for the rest cycles. (c) Charge/discharge capacity of four electrodes over 100 cycles: Si film (black squares), CNS/Si with Si mass percent of 22.1% (red circles), 62.9% (blue triangles) and CNS/Si/Al₂O₃ with Si mass percent of 62.5% (green stars). (d) Charge/discharge capacity and Coulombic efficiency of CNS/Si/Al₂O₃ at high current densities ranging from 0.5 A g⁻¹ to 8 A g⁻¹.

composites shown in Supplementary Fig. S1 we can also see that the initial capacities were similar, but CNS/Si/Al₂O₃ possessed the highest capacity retention after 100 cycles. When different current densities of 0.2 A g⁻¹ and 4 A g⁻¹ were applied to the battery test, CNS/Si/Al₂O₃ still showed great electrochemical performance (Supplementary Fig. S2). Therefore, we can ensure to say that under the combined action of the hollow CNS substrate, surface-to-surface contact mode and Al₂O₃ coating, our sample presented high specific capacity and remarkable capacity retention simultaneously, which demonstrated the superior design of our structure.

Figure 5d shows the outstanding rate performance of CNS/Si/Al₂O₃, where the current densities ranged from 0.5 to 8 A g⁻¹. Even at a rate of 8 A g⁻¹, the CNS/Si/Al₂O₃ electrode can still achieve a discharge capacity of 854 mA h g⁻¹, comparable to the previous reports^{25–29}. When the current density was altered from 8 A g⁻¹ back to 0.5 A g⁻¹, the capacity was fully recovered. This implied that the structural stability was retained during cycling. The Coulombic efficiency increased from 81.0% at the first cycle to 99.0% at the ninth cycle, and then stayed above 99% thereafter. The Coulombic efficiency gradually increased as the current density increased. This was caused by the smaller volume expansion of Si under high current density, rendering the SEI more stable.

SEM images of CNS/Si and CNS/Si/Al₂O₃ after charge/discharge for 100 cycles are respectively displayed in Fig. 6a and 6b. To observe the pristine morphology, SEI layers were not removed from the surface of electrodes. The size of the CNS/Si structure units became much larger due to the thick SEI formation. Several original structure units could be wrapped together inside the SEI, making the structure

look coarser. Cracks still remained on the film. However, the width of some cracks got bigger due to the Si volume change. By comparison, the structure of CNS/Si/Al₂O₃ looked much finer, which provided the visualized evidence of the suppressed electrolyte decomposition. Figure 6c and 6d display the SEM and TEM images of CNS/Si/Al₂O₃ after 100 cycles and removing SEI with diluted HCl (Al₂O₃ layer was removed by the acid, as shown in Supplementary Fig. S4). The surface of Si became rougher compared to that before cycling. However, Si was neither pulverized nor detached from CNSs, demonstrating that our design can efficiently accommodate the volume expansion of Si and maintain the integrity of the structure, as proved in the rate performance (Fig. 5d).

Discussion

In order to understand the great battery performance, we conducted the electrochemical impedance spectroscopy (EIS) measurement of CNS/Si and CNS/Si/Al₂O₃ before and after 100 charge/discharge cycles (Fig. 7). The two curves after cycling were composed of two partially overlapped depressed semicircles in the high-to-medium frequency range and a low frequency sloping line. Such a pattern of the EIS can be fitted by an equivalent circuit shown in the inset, where R_b was the bulk resistance of the cell, which reflected the electric conductivity of electrolyte, separator and electrodes; R_{sei} and C_{sei} were the resistance and capacitance of SEI, which corresponded to the first semicircle at high frequency; R_{ct} and C_{dl} were the charge transfer resistance and its relative double-layer capacitance, which corresponded to the second semicircle at medium frequency; W was the Warburg impedance related to the diffusion effect

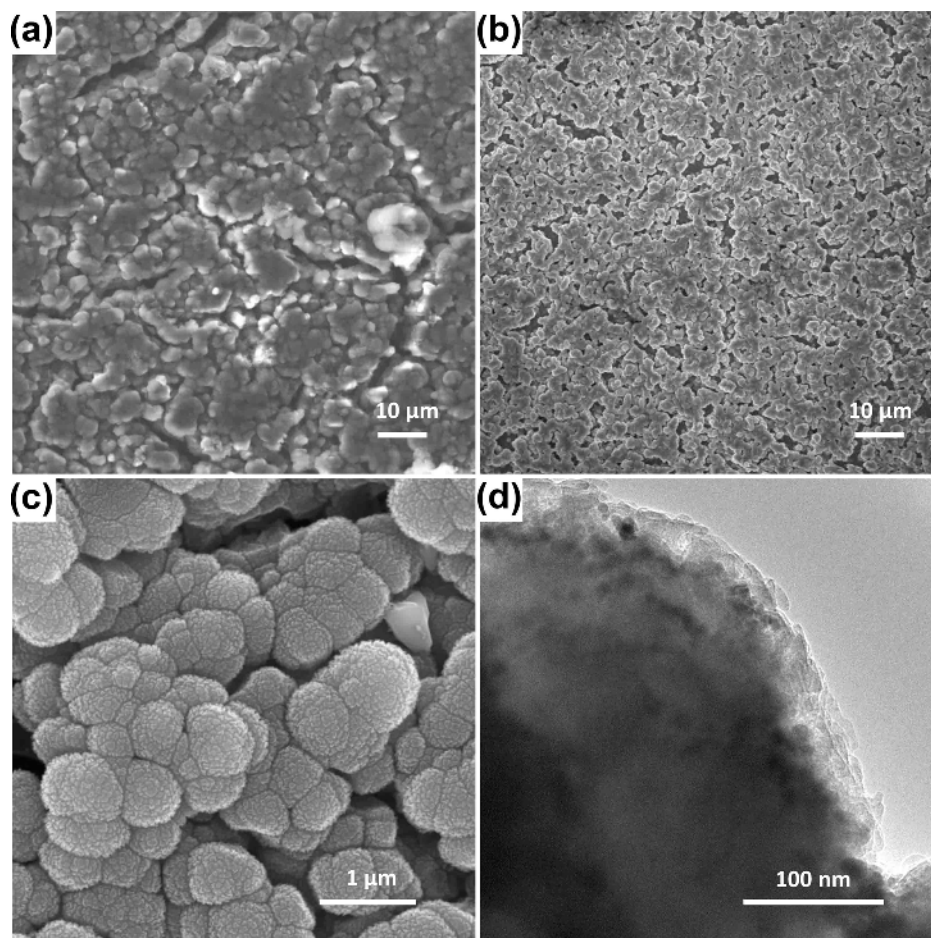


Figure 6 | SEM and TEM characterization of the electrodes after cycling. SEM images of (a) CNS/Si and (b) CNS/Si/Al₂O₃ after 100 cycles test without the removal of SEI. (c) SEM and (d) TEM images of CNS/Si/Al₂O₃ after 100 cycles test and removing SEI with HCl.

of Li⁺, which was generally indicated by a sloping line at low frequency^{47,48}. The curves before cycling contained only one semicircle related to R_{ct} and C_{dl} because no SEI was formed. The results revealed that before cycling both R_b and R_{ct} were almost the same between the two electrodes: ~2 Ω and ~51 Ω. The small R_b proved the high conductivity of the electrodes and good connection between CNSs and the current collectors. R_{ct} also had a relatively low value com-

pared to others' results as shown in Table 1, indicating the facile charge transfer process at the interface between Si and the electrolyte. R_b and R_{ct} almost had no change after Al₂O₃ deposition, suggesting that the ALD layer did harm to neither the conductivity of the electrodes nor the charge transfer reaction. After charge/discharge for 100 cycles, the shape of the EIS for CNS/Si changed a lot. The curve contained two partially overlapped depressed semicircles, and the diameters of the two semicircles were fairly large, which was a strong evidence of thick SEI formation. Though SEI was an ion conductor and electron insulator, its ionic conductivity was much smaller than that of the state-of-the-art liquid electrolyte⁴⁶. Thus, thick SEI layer could increase the ionic and electronic resistance and harm the charge transfer process at the Si-SEI interface, leading to the increased R_{ct} (~121 Ω). Nevertheless, for CNS/Si/Al₂O₃ after cycling, the diameters of the two semicircles were much smaller. As mentioned above, Li⁺ conducting LiAlO₂ thin layer was formed during lithiation, which helped reduce the energy barrier for Li⁺ insertion and enhance the charge transfer kinetics²², and the decomposition of electrolyte was significantly suppressed by the Al₂O₃ coating. As a consequence, R_b and R_{sei} were smaller than that of CNS/Si, and R_{ct} just slightly increased.

Compared to previous works with relevant structures listed in Table 1, the overall performance (current density applied, specific capacity and capacity retention) of our structure was much superior to most of them or comparable to the best designed structures. The advantages of our structure over others have led to the outstanding performance. No binder or carbon black additives were used in our structure, which simplified the fabrication process and reduced the weight of the electrodes. Most of all, our structure combined several

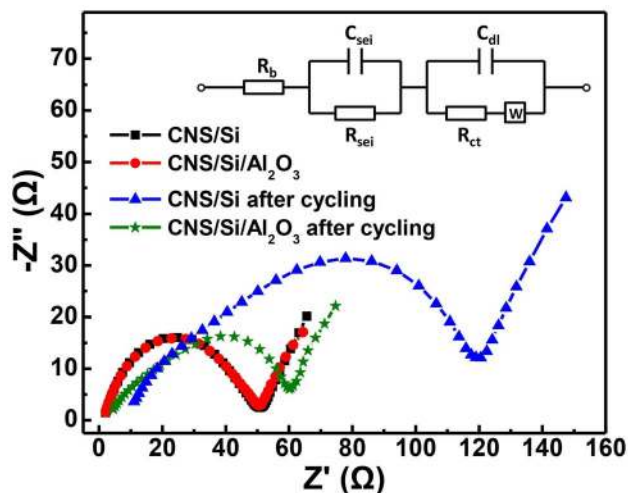


Figure 7 | EIS of CNS/Si and CNS/Si/Al₂O₃ before and after charge/discharge test. The equivalent circuit is shown in the inset.



Table 1 | Anode performance comparison of recent works about relevant Si/C structure

Structure	Method	Si mass percent	R_{ct} @ cycles [Ω]	Current density [$A\ g^{-1}$]	Capacity @ cycles [$mA\ h\ g^{-1}$]	Capacity retention
Hollow CNS/Si/Al₂O₃ (Ours)	PECVD	62.5%	51 @ 0 60 @ 100	1	1560 @ 100	84.8%
Si@void@Carbon tubes ²⁵	Electrospinning	47%	-	1	870 @ 200	90%
Si@void@C ²⁶	Chemical Etching	71%	~1000 @ 0 ~150 @ 10	4.2	1300 @ 1000	74%
Si@void@C ²⁷	Chemical Etching	48%	-	0.2	1625 @ 100 ^{a)}	69%
Si@void@C ²⁸	Electroless Etching	63%	-	0.2	1500 @ 50	79%
SiNW@void@graphitic tubes ²⁹	CVD	70%	-	4.2	1100 @ 1000	63%
Si@Graphene ³⁰	Electrostatic Attraction	80.1%	28 @ 0 75 @ 150	0.1	1205 @ 150	73%
Si/B ₄ C/Graphite ³¹	Ball Milling	57%	100 @ 1	0.63	680 @ 200	78.5%
Aligned CNT/Si sheet ³²	CVD	60–70%	-	0.1	1494 @ 45	94%
Rolled-Up C/Si/C ³³	Sputtering	40%	-	0.5	1000 @ 300	1
Twisted MWCNT/Si fiber ³⁴	E-beam Evaporation	38.1%	185 @ 0 68 @ 30 140 @ 0	1	1000 @ 50	61%
Si/AlGI ³⁵	Molecular Layer Deposition	1	140 @ 0	0.1 C ^{b)}	900 @ 150	55%

^{a)}Capacity was calculated based on Si mass;
^{b)}C rate was not mentioned in the reference.

main factors together for high performance LIBs, which were void space around Si accommodating volume change, protective coatings suppressing the electrolyte decomposition, interconnected 3D conductive substrates and surface-to-surface contact mode enabling fast electron transport. None of the previous designs shown in the table could satisfy the above factors simultaneously.

In summary, we have successfully designed a novel CNS/Si/Al₂O₃ nanostructure for high performance LIBs. Hollow CNSs were synthesized by template-directed carbon segregation method, and CNS 3D substrate was fabricated by electrophoretic deposition technique. CNS/Si/Al₂O₃ core-shell film was eventually obtained by depositing Si with PECVD and Al₂O₃ with ALD. As-fabricated structure was able to overcome the typical issues of Si anode LIBs and has demonstrated outstanding battery performance. CV measurement revealed the electrochemical stability of our structure due to the hollow CNS substrate. The long term charge/discharge test showed that the cycling stability decreased with the increasing mass percent of Si in the CNS/Si electrode, while it can be improved again by Al₂O₃ coating. As a result, CNS/Si/Al₂O₃ exhibited high specific capacity and excellent capacity retention over 100 cycles. Moreover, the rate performance also manifested good rate capability. The structural stability was further confirmed by EIS measurement and visualized observation of SEM and TEM images.

Methods

Preparation of Hollow CNSs. Ni-NPs were prepared by reducing NiCl₂ in aqueous solution. The prepared Ni-NPs were transferred into triethylene glycol (TEG, ReagentPlus®, Sigma Aldrich) which contained a small amount of NaOH aqueous solution. Keeping the system at 220 °C for 12 h finally led to the formation of carbon-incorporated Ni-NPs. The prepared samples were placed in a furnace and annealed in an argon atmosphere at 500 °C for 1 h, resulting in Ni-C core-shell structure. The hollow CNSs were obtained by dissolving the core Ni-NPs in a dilute HCl solution for 12 h.

Fabrication of CNS Film on Stainless Steel. Hollow CNSs were made hydrophilic by dissolving and sonicating in a 3:1 (v/v) mixture of concentrated H₂SO₄ and HNO₃ for 10 min in a bath-type sonicator (RK 106, Bandelin Electronic, Germany), followed by vigorous stirring at 70 °C for 40 min. The functionalized CNSs were dispersed in ethanol by homogenizing for 40 min and centrifuging at 2000 rpm for 20 min. In order to charge the CNSs, a small amount of Mg(NO₃)₂·6H₂O (Puriss. p.a. Sigma Aldrich) were added into the suspension. Two stainless steel foils were used as electrophoretic deposition electrodes, and were put into the suspension and kept parallel. A dc voltage of 30 V (HYP-303D, Han Young Electronic Co. South Korea) was applied on the electrodes and thus the charged CNSs were attracted towards the cathode. The samples were dried at 120 °C in a vacuum oven for 12 h.

Fabrication of CNS/Si. The samples were cut into 1 × 1 cm² and loaded in a PECVD reactor (A-Tech, South Korea). During the temperature increasing from room temperature to 300 °C, H₂ was introduced and the plasma was switched on (H₂ flow: 20 sccm; pressure: 60 mTorr; RF power: 20 W). At 300 °C, SiH₄ was introduced (SiH₄ flow: 2 sccm) for the deposition of Si during 5 h. After the termination of deposition and temperature decreased to room temperature, the samples were unloaded and immediately transferred into the Ar-filled glove box.

Fabrication of CNS/Si/Al₂O₃. The samples were loaded into the ALD apparatus (Lucida D100, NCD Technology, South Korea) for Al₂O₃ deposition at 150 °C (50 cycles). Trimethyl aluminium and water were used as Al₂O₃ precursors and N₂ as the carrier gas. After the termination of deposition and temperature decreased to room temperature, the samples were unloaded and immediately transferred into the Ar-filled glove box.

Material Characterization. The morphology and structure of the synthesized and electrochemically tested samples were observed by SEM (JEOL, FESEM 7600F) and TEM (JEOL, JEM 3010, 300 kV). The samples were directly used for SEM observations. For TEM observations, the samples were firstly sonicated in ethanol and then transferred onto holey carbon membranes supported by copper grids. Raman spectroscopy (Renishaw, RM-1000 Invia) with an excitation energy of 2.41 eV (514 nm, Ar⁺ ion laser) was used to characterize the optical properties of the samples.

Electrochemical Measurement. The mass ratio of each component of the electrodes was determined by carefully weighing the samples step by step using the A&D BM-22 microbalance located inside the dry room. The mass loading was about 0.3 mg cm⁻². The cell was assembled in a dry room using CR 2032 cell case with Si film, CNS/Si or CNS/Si/Al₂O₃ on a stainless steel foil as the working electrode, a lithium metal foil as the counter/reference electrode, and 1 M of LiPF₆ in a 1:1 (v/v) mixture of ethylene carbonate (EC) and diethyl carbonate (DEC) as the electrolyte. A glassy carbon microfiber was used as the separator. Electrochemical measurements were carried out using VMP3 instrument (BioLogic Science Instruments). The cells were charged and discharged galvanostatically between 1.0 and 0.01 V vs. Li/Li⁺. The CV measurement of the half cell battery was performed at a rate of 0.1 mV s⁻¹. The EIS curves were obtained by applying a sine wave with an amplitude of 10 mV over a frequency range of 100 kHz to 10 mHz to the assembled cells before and after cycling.

- Reddy, A. L. M., Gowda, S. R., Shaijumon, M. M. & Ajayan, P. M. Hybrid nanostructures for energy storage applications. *Adv. Mater.* **24**, 5045–5064 (2012).
- Kim, M. G. & Cho, J. Reversible and high-capacity nanostructured electrode materials for Li-ion batteries. *Adv. Funct. Mater.* **19**, 1497–1514 (2009).
- Li, H., Wang, Z., Chen, L. & Huang, X. Research on advanced materials for Li-ion batteries. *Adv. Mater.* **21**, 4593–4607 (2009).
- Yao, F. *et al.* Diffusion mechanism of lithium ion through basal plane of layered graphene. *J. Am. Chem. Soc.* **134**, 8646–8654 (2012).
- Chockla, A. M. *et al.* Silicon nanowire fabric as a lithium ion battery electrode material. *J. Am. Chem. Soc.* **133**, 20914–20921 (2011).
- Jeong, S. *et al.* Etched graphite with internally grown Si nanowires from pores as an anode for high density Li-ion batteries. *Nano Lett.* **13**, 3403–3407 (2013).



7. Chan, C. K. *et al.* High-performance lithium battery anodes using silicon nanowires. *Nat. Nanotechnol.* **3**, 31–35 (2008).
8. Nguyen, H. T. *et al.* Alumina-coated silicon-based nanowire arrays for high quality Li-ion battery anodes. *J. Mater. Chem.* **22**, 24618–24626 (2012).
9. Wu, H. *et al.* Stable cycling of double-walled silicon nanotube battery anodes through solid–electrolyte interphase control. *Nat. Nanotechnol.* **7**, 310–315 (2012).
10. Martin, C. *et al.* Chemical coupling of carbon nanotubes and silicon nanoparticles for improved negative electrode performance in lithium-ion batteries. *Adv. Funct. Mater.* **21**, 3524–3530 (2011).
11. Zhao, X., Hayner, C. M., Kung, M. C. & Kung, H. H. In-plane vacancy-enabled high-power Si–graphene composite electrode for lithium-ion batteries. *Adv. Energy Mater.* **1**, 1079–1084 (2011).
12. Zhao, C. *et al.* Coaxial carbon–silicon–carbon nanotube arrays in porous anodic aluminum oxide templates as anodes for lithium ion batteries. *J. Mater. Chem.* **22**, 12193–12197 (2012).
13. Yoo, J. K., Kim, J., Jung, Y. S. & Kang, K. Scalable fabrication of silicon nanotubes and their application to energy storage. *Adv. Mater.* **24**, 5452–5456 (2012).
14. Li, X. *et al.* Carbon nanotube-enhanced growth of silicon nanowires as an anode for high-performance lithium-ion batteries. *Adv. Energy Mater.* **2**, 87–93 (2012).
15. Nguyen, H. T. *et al.* Highly interconnected Si nanowires for improved stability Li-ion battery anodes. *Adv. Energy Mater.* **1**, 1154–1161 (2011).
16. Yao, Y. *et al.* Interconnected silicon hollow nanospheres for lithium-ion battery anodes with long cycle life. *Nano Lett.* **11**, 2949–2954 (2011).
17. Cui, L. F., Yang, Y., Hsu, C. M. & Cui, Y. Carbon-silicon core-shell nanowires as high capacity electrode for lithium ion batteries. *Nano Lett.* **9**, 3370–3374 (2009).
18. Yao, F. *et al.* A strategy of overcoming the limit of carbon-based materials for anode of lithium ion battery. *Carbon* **79**, 563–571 (2014).
19. Abel, P. R., Lin, Y. M., Celio, H., Heller, A. & Mullins, C. B. Improving the stability of nanostructured silicon thin film lithium-ion battery anodes through their controlled oxidation. *ACS Nano* **6**, 2506–2516 (2012).
20. Yin, Y. X., Xin, S., Wan, L. J., Li, C. J. & Guo, Y. G. Electro spray synthesis of silicon/carbon nanoporous microspheres as improved anode materials for lithium-ion batteries. *J. Phys. Chem. C* **115**, 14148–14154 (2011).
21. Cao, F. F. *et al.* Cu-Si nanocable arrays as high-rate anode materials for lithium-ion batteries. *Adv. Mater.* **23**, 4415–4420 (2011).
22. Xiao, X., Lu, P. & Ahn, D. Ultrathin multifunctional oxide coatings for lithium ion batteries. *Adv. Mater.* **23**, 3911–3915 (2011).
23. He, Y., Yu, X., Wang, Y., Li, H. & Huang, X. Alumina-coated patterned amorphous silicon as the anode for a lithium-ion battery with high coulombic efficiency. *Adv. Mater.* **23**, 4938–4941 (2011).
24. McDowell, M. T., Lee, S. W., Wang, C. & Cui, Y. The effect of metallic coatings and crystallinity on the volume expansion of silicon during electrochemical lithiation/delithiation. *Nano Energy* **1**, 401–410 (2012).
25. Wu, H. *et al.* Engineering empty space between Si nanoparticles for lithium-ion battery anodes. *Nano Lett.* **12**, 904–909 (2012).
26. Liu, N. *et al.* A Yolk-shell design for stabilized and scalable Li-ion battery alloy anodes. *Nano Lett.* **12**, 3315–3321 (2012).
27. Chen, S. *et al.* Silicon core–hollow carbon shell nanocomposites with tunable buffer voids for high capacity anodes of lithium-ion batteries. *Phys. Chem. Chem. Phys.* **14**, 12741–12745 (2012).
28. Park, Y. *et al.* Si-encapsulating hollow carbon electrodes via electroless etching for lithium-ion batteries. *Adv. Energy Mater.* **3**, 206–212 (2013).
29. Wang, B. *et al.* Contact-engineered and void-involved silicon/carbon nanohybrids as lithium-ion-battery anodes. *Adv. Mater.* **25**, 3560–3565 (2013).
30. Zhou, X., Yin, Y. X., Wan, L. J. & Guo, Y. G. Self-assembled nanocomposite of silicon nanoparticles encapsulated in graphene through electrostatic attraction for lithium-ion batteries. *Adv. Energy Mater.* **2**, 1086–1090 (2012).
31. Chen, X. *et al.* Conductive rigid skeleton supported silicon as high-performance Li-ion battery anodes. *Nano Lett.* **12**, 4124–4130 (2012).
32. Fu, K. *et al.* Aligned carbon nanotube-silicon sheets: a novel nano-architecture for flexible lithium ion battery electrodes. *Adv. Mater.* **25**, 5109–5114 (2013).
33. Deng, J. *et al.* Naturally rolled-up C/Si/C trilayer nanomembranes as stable anodes for lithium-ion batteries with remarkable cycling performance. *Angew. Chem. Int. Ed.* **52**, 2326–2330 (2013).
34. Lin, H. *et al.* Twisted aligned carbon nanotube/silicon composite fiber anode for flexible wire-shaped lithium-ion battery. *Adv. Mater.* **26**, 1217–1222 (2014).
35. Piper, D. M. *et al.* Reversible high-capacity Si nanocomposite anodes for lithium-ion batteries enabled by molecular layer deposition. *Adv. Mater.* **26**, 1596–1601 (2014).
36. Choi, J. Y. *et al.* A chemical route to large-scale preparation of spherical and monodisperse Ni powders. *J. Am. Ceram. Soc.* **88**, 3020–3023 (2005).
37. Yoon, S. M. *et al.* Synthesis of multilayer graphene balls by carbon segregation from nickel nanoparticles. *ACS Nano* **6**, 6803–6811 (2012).
38. Du, C. & Pan, N. Supercapacitors using carbon nanotubes films by electrophoretic deposition. *J. Power Sources* **160**, 1487–1494 (2006).
39. Casiraghi, C., Pisana, S., Novoselov, K. S., Geim, A. K. & Ferrari, A. C. Raman fingerprint of charged impurities in graphene. *Appl. Phys. Lett.* **91**, 233108 (2007).
40. Holzapfel, M. *et al.* Nano silicon for lithium-ion batteries. *Electrochim. Acta* **52**, 973–978 (2006).
41. Kanellis, G., Morhange, J. F. & Balkanski, M. Effect of dimensions on the vibrational frequencies of thin slabs of silicon. *Phys. Rev. B* **21**, 1543–1548 (1980).
42. Smith, J. E., Brodsky, M. H., Crowder, B. L., Nathan, M. I. & Pinczuk, A. Raman spectra of amorphous Si and related tetrahedrally bonded semiconductors. *Phys. Rev. Lett.* **26**, 642–646 (1971).
43. Nakamoto, K. [Chapter 2. Applications in inorganic chemistry] *Infrared and Raman spectra of inorganic and coordination compounds: Part A: Theory and applications in inorganic chemistry* [Sixth edition] [276–278] (John Wiley & Sons, Inc., Hoboken, NJ, USA, 2009).
44. Xiao, Y., Hao, D., Chen, H., Gong, Z. & Yang, Y. Economical synthesis and promotion of the electrochemical performance of silicon nanowires as anode material in Li-ion batteries. *ACS Appl. Mater. Interfaces* **5**, 1681–1687 (2013).
45. McDowell, M. T., Lee, S. W., Nix, W. D. & Cui, Y. 25th anniversary article: understanding the lithiation of silicon and other alloying anodes for lithium-ion batteries. *Adv. Mater.* **25**, 4966–4985 (2013).
46. Li, J., Xiao, X., Cheng, Y. T. & Verbrugge, M. W. Atomic layered coating enabling ultrafast surface kinetics at silicon electrodes in lithium ion batteries. *J. Phys. Chem. Lett.* **4**, 3387–3391 (2013).
47. Zhang, S. S., Xu, K. & Jow, T. R. Electrochemical impedance study on the low temperature of Li-ion batteries. *Electrochim. Acta* **49**, 1057–1061 (2004).
48. Wang, C., Appleby, A. J. & Little, F. E. Electrochemical impedance study of initial lithium ion intercalation into graphite powders. *Electrochim. Acta* **46**, 1793–1813 (2001).

Acknowledgments

This work was supported by Institute for Basic Science (IBS-R011-D1) and in part by BK21-Plus through Ministry of Education, Korea.

Author contributions

B.L., F.Y. and J.J.B. devised the original concept and designed the experiments. B.L. performed the electrochemical experiments and wrote the paper. J.C., M.R.Z. and D.T.L. carried out the PECVD fabrication of Si. B.L., F.Y., D.T.P. and H.Y. analyzed the data. Y.H.L. supervised the research and revised the manuscript. All authors discussed the results and commented on the manuscript.

Additional information

Supplementary information accompanies this paper at <http://www.nature.com/scientificreports>

Competing financial interests: The authors declare no competing financial interests.

How to cite this article: Li, B. *et al.* Hollow carbon nanospheres/silicon/alumina core-shell film as an anode for lithium-ion batteries. *Sci. Rep.* **5**, 7659; DOI:10.1038/srep07659 (2015).



This work is licensed under a Creative Commons Attribution-NonCommercial-NoDerivs 4.0 International License. The images or other third party material in this article are included in the article's Creative Commons license, unless indicated otherwise in the credit line; if the material is not included under the Creative Commons license, users will need to obtain permission from the license holder in order to reproduce the material. To view a copy of this license, visit <http://creativecommons.org/licenses/by-nc-nd/4.0/>